Resolving Cellular Morphology in the Human Brain with Multiparametric Diffusion MR Spectroscopy

André Döring[1,2,✉], Frank Rösler[3], Kadir Şimşek[2], Maryam Afzali[4,5,2], Roland Kreis[6,7], Karl Landheer[8,9], Derek K Jones[2], Julien Valette[10], and Marco Palombo[2,11]

[1]CIBM Center for Biomedical Imaging, EPFL CIBM-AIT, Lausanne, Switzerland
[2]Cardiff University Brain Research Imaging Centre (CUBRIC), School of Psychology, Cardiff University, Cardiff, United Kingdom
[3]Department of Mathematics, University of Bern, Bern, Switzerland
[4]Department of Cardiovascular Sciences, University of Leicester and the National Institute for Health Research (NIHR), Leicester Biomedical Research Centre, Leicester, United Kingdom
[5]Leeds Institute of Cardiovascular and Metabolic Medicine, University of Leeds, Leeds, United Kingdom
[6]Magnetic Resonance Methodology, Institute of Diagnostic and Interventional Neuroradiology, University Bern, Bern, Switzerland
[7]Translational Imaging Center, sitem-insel, Bern, Switzerland
[8]Department of Biomedical Engineering, Columbia University, New York, USA
[9]Regeneron Genetics Center, Tarrytown, New York, USA
[10]Laboratoire des Maladies Neurodégénératives, Université Paris-Saclay, CEA, CNRS, MIRCen, Fontenay-aux-Roses, France
[11]School of Computer Science and Informatics, Cardiff University, Cardiff, United Kingdom

Diffusion-weighted magnetic resonance spectroscopy (dMRS) is a unique, non-invasive technique capable of probing cell-type specific morphology. However, conventional dMRS methods are limited in their ability to provide detailed morphological information. This study demonstrates the potential of a multi-parametric dMRS approach, combining diffusion-time dependent and double-diffusion encoding MR spectroscopy, to characterize soma and neurite morphology of neuronal and glial cells. This methodology holds promise for developing biomarkers for the diagnosis, monitoring, and phenotyping of neurological pathologies, like Alzheimer's Disease, Parkinson's Disease, or Multiple Sclerosis, where alterations in soma and neurite morphology are reported.

MR spectroscopy | diffusion | multiparametric | microstructure | diffusion-time encoding | double-diffusion encoding

Correspondence: ***andre.doring@epfl.ch***

Introduction

Diffusion-weighted magnetic resonance spectroscopy (dMRS) is a unique MR modality that allows measuring metabolite diffusion non-invasively *in vivo* in the human brain(1–4). Unlike water, most metabolites are confined to intracellular spaces, wherein specific metabolites predominantly inhabit distinct cell types. Metabolite diffusion characteristics can thus serve as a probe to study selectively neuronal (e.g., N-acetylaspartate [NAA] and glutamate [Glu]) and glial (e.g., myo-inositol [mI] and choline-containing compounds [tCho]) microstructure(4, 5).

In recent years, advances in diffusion modelling have significantly improved the prediction of MR signals for specific cellular morphologies. However, the challenge of solving the inverse problem – reconstructing cellular morphology from MR diffusion signals – remains for two particular reasons: (i) modelling of the diffusion signal in realistic cellular structures necessitates time-consuming simulations (e.g., Monte Carlo), thereby impeding an efficient implementation of inverse fitting routines, and (ii) traditional dMRS experiments sample diffusion signals in a low dimensional space, resulting in ambiguous solutions which, at best, can recover basic morphological features (e.g., standard model of dMRS composed of one compartment of fully dispersed cylinders).

In this work, we combine the measurement of metabolite diffusion at various diffusion-times (TDs) with double-diffusion-encoding spectroscopy (DDES) based on multi-directional encoding.

Depending on TD, apparent diffusion coefficients (ADC) and diffusion kurtosis (K) are affected by different dimensions of cellular barriers(6). Pulsed gradient (PG) diffusion-encoding is commonly used to measure at long TD ($\geq$ 50 ms) where ADCs and Ks represent diffusion mostly along tortuous cellular fibers(7–9). Oscillating gradient (OG) diffusion-encoding is used at short TD ($\leq$ 10 ms), where ADCs and Ks have higher sensitivity to small cellular –including subcellular– properties (e.g., cytoplasmic viscosity, fiber diameter, soma dimension)(6, 10, 11). One can categorize dMRS techniques according to the targeted TDs, where stimulated-echo sequences (e.g., STEAM) are applied with PG at long TD and spin-echo sequences (e.g., semiLASER, PRESS) at short (with OG) to intermediate (with PG) TD. Fig. 1a shows a representative overview of the used sequences and diffusion-encoding strategies for the particular diffusion-time intervals.

Current dMRS techniques are mostly applied at long TDs focused on high diffusion-weighting. For instance, by increasing b-values gradually up to 8 ms µm^{-2} one can infer the deviation from a monoexponential diffusion decay, which gives access to the kurtosis (K), which is the second-order term in the signal's cumulant expansion(12).

However, at short TD ($\leq$ 10 ms), the maximum achievable diffusion-weighting in human experiments is limited by peripheral and cardiac nerve stimulation (PNS/CNS), gradient-slew-rate and forbidden acoustic frequencies, which prevents measuring K(TD). Thus, in this short TD range, usually only ADC(TD) is accessible in humans. Yet to increase the sampled parameter space, gathering ADC(TD) from short

DRAFT

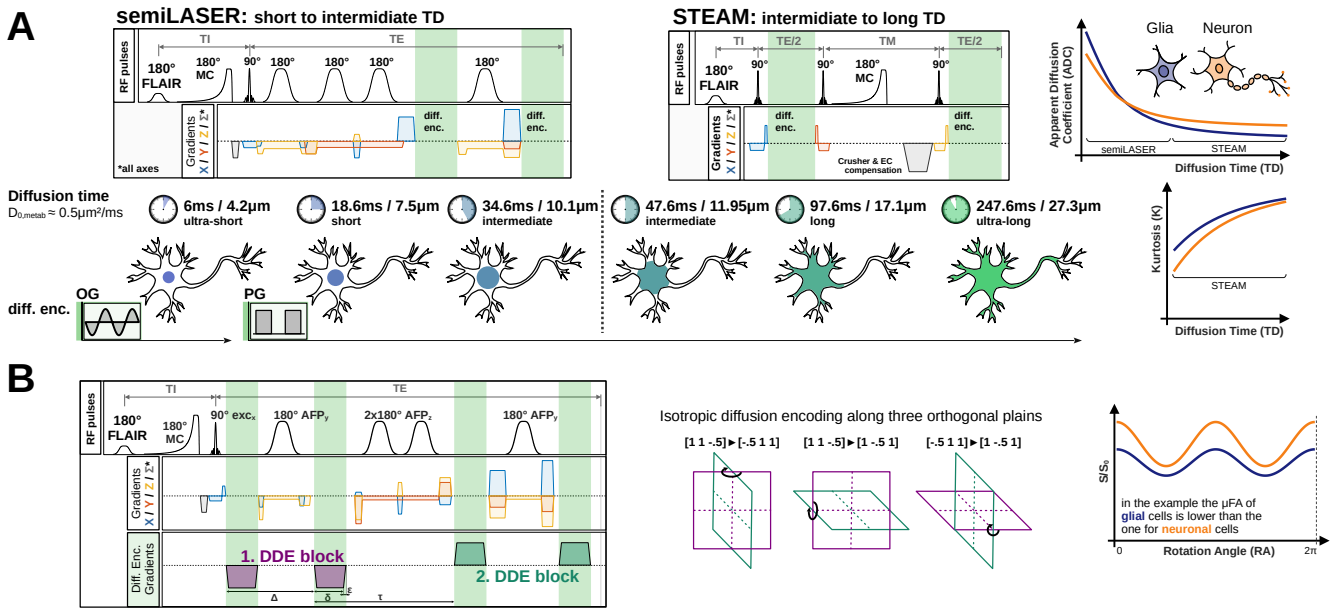

Fig. 1: **Acquisition strategies:** (A) STEAM and semiLASER sequences were used to measure the diffusion-time (TD) dependence of the apparent diffusion coefficient (ADC) and diffusion kurtosis (K). In the short TD range (6, 21, 37 ms) semiLASER was used up to a b-value of $3\,\mathrm{ms\,\mu m^{-2}}$ with oscillating gradients [OG] at the shortest TD and pulsed gradients [PG] otherwise. In the long TD range (50, 100, 250 ms) STEAM was used up to a b-value of $8\,\mathrm{ms\,\mu m^{-2}}$ with PG encoding. (B) The semiLASER sequence was extended with double diffusion-encoding (DDE) gradient pairs. DDE was applied in three orthogonal planes to achieve a powder averaged diffusion encoding. The STEAM and semiLASER sequences are both equipped with metabolite-cycling (MC) to measure water and metabolite diffusion simultaneously and fluid attenuated inversion recovery (FLAIR) to suppress cerebrospinal fluid (CSF).

TD (milliseconds) to intermediate and long TD (tens and hundreds of milliseconds) still enables microstructural information to be recovered(6, 13, 14). Indeed, ADC(TD) is directly affected by cellular characteristics at different length-scales (e.g., cytoplasmic viscosity, molecular crowding, intracellular organelles, tortuosity and barriers, and fibre dimension)(10, 15). Although, as presented in mice, the TD dependence of K(TD) benefits microstructural modelling, it is only accessible in a restricted TD range > 50 ms in humans due to aforementioned limitations(16).

On the other hand, DDE uses two-dimensional diffusion-encoding with varying angles between two pairs of diffusion-encoding gradients as presented in Fig. 1b. This allows distinguishing between microscopic compartments such as cylinders and spheres in a macroscopically amorphous tissue environment(17). Double-Diffusion-Encoded Spectroscopy (DDES) may thus provide cell-specific microstructural information.

So far, such multi-parametric diffusion-weighted spectroscopy has been limited to animal studies. In this work, we combine both techniques – diffusion-time dependence and double-diffusion encoding – in a human cohort. We measure the diffusion-time dependence of the ADC(TD) in the low b-value range up to $3\,\mathrm{ms\,\mu m^{-2}}$ over a wide range of TDs from 6 ms to 250 ms. In a higher b-value range of up to $8\,\mathrm{ms\,\mu m^{-2}}$ we also estimate the K(TD) dependence for TDs ranging from 50 ms to 250 ms. Moreover, we acquire DDES data in an 8-step gradient rotation cycle at a b-value of $5.2\,\mathrm{ms\,\mu m^{-2}}$. We use the combined multi-parametric dataset to inform cell-structural models to estimate cell-specific microstructural features and to compensate for model ambiguities.

First, TD and DDES data were fitted separately to a two-compartment tissue model to directly retrieve cellular morphologies of soma (R_s) and neurite (R_c) radii, the compartmental fraction of neurites (f_c) and the intrinsic diffusivity (D_0). Moreover, DDES data alone were fitted using a tensor model to reveal information on the microscopic fractional anisotropy (μFA), axial ($D_{\parallel}$) and radial ($D_{\perp}$) diffusion coefficients along the predominant fibre direction, and the mean diffusivity (MD). Second, we implement multi-parametric dMRS fitting TD and DDES data jointly.

The aim of this work is to: (i) demonstrate that metabolite ADC(TD) and K(TD) dependence can be observed; (ii) explore to what extent DDES can provide complementary information; and (iii) investigate the usage of multi-parametric tissue modeling to enhance the estimation accuracy of cell-specific microstructural features.

For this purpose, we exploit state-of-the-art dMRS sequences and ultra-strong gradients on a Connectom MR scanner combined with experiments on clinical 3T scanners.

The first part of this work presents our results on the estimation of morphological cell-specific features from applying either diffusion-time dependent or double-diffusion-encoded MR spectroscopy alone. Subsequently, we combine both methods, showing an improvement in model stability by joint fitting of diffusion-time dependence and double-diffusion encoding. We close with a discussion suggesting specific dMRS protocol configurations and potential pathways to further improve microstructural sensitivity.

Results

Diffusion-weighted spectra. Fig. 2 shows exemplary diffusion-weighted spectra of the diffusion-time (A) and

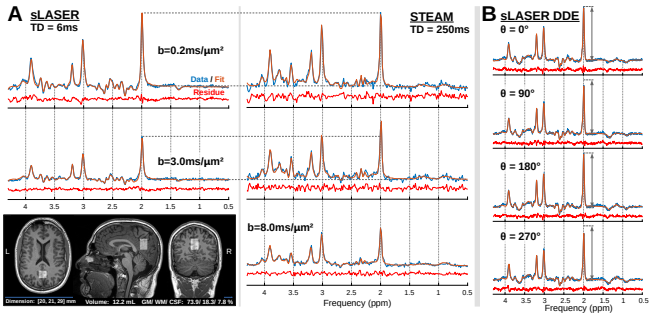

Fig. 2: **Spectral quality and fitting:** (A) Shows the results from spectral fitting at the shortest diffusion-time (6 ms) for semiLASER (left) at b-values of 0.2 and 3.0 ms µm^{-2} and the longest diffusion-time (250 ms) for STEAM (right) at b-values of 0.2, 3.0 and 8.0 ms µm^{-2} (left corner: voxel position in occipital gray matter). Spectra at the lowest b-value are scaled to equal NAA peak height with faster NAA diffusion at the shortest diffusion-time evident from the stronger signal attenuation. (B) Shows the results from spectral fitting of the DDES experiment at four selected rotation angels. The NAA peak height is scaled to the rotation angle at 0° showing the modulation of the NAA peak intensity. In all experiments linear-combination-modelling (orange) and residuals (red) report good fitting quality.

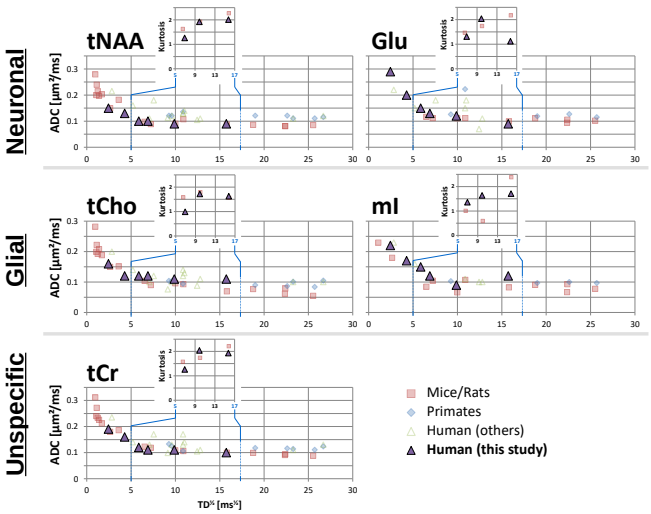

Fig. 3: **Literature comparison:** Dependence of $ADC_E(TD)$ and $K(TD)$ for specific brain metabolites in comparison to other studies in rodents (□), primates (◇) and humans (△). (Data source: (8, 10, 11, 13, 16, 19–28))

double-diffusion encoding (B) experiments, in a single subject with the voxel placed midline in the posterior cingulate cortex (PCC). In both cases, spectra are free from eddy-current artifacts and residual water, giving an overall spectral quality well in line with consensus recommendations(18).

The spectra in Fig. 2a were acquired at the shortest and longest diffusion-times, i.e.,6 and 250 ms, respectively. The cohort-wide signal-to-noise ratio (SNR) relative to the NAA peak intensity at b =3 ms µm^{-2} is 36.8±9.0 and 45.8±6.8 for semi-LASER and STEAM, respectively, and above the minimum consensus recommendation for dMRS(18). The linewidth of the NAA peak increased slightly towards higher b-values for both semiLASER and STEAM with mean values of (4.7±0.6) and (4.5 ± 0.5) Hz, respectively (averaged over all b-values, TDs and subjects). For visual comparison, spectra at 6 and 250 ms are scaled for equal NAA peak heights at the lowest b-value. Faster NAA diffusion at the shortest diffusion-time of 6 ms is directly evident from a stronger signal attenuation at $b = 3$ ms µm^{-2} (note: other metabolite peaks cannot be compared directly due to metabolite specific T2s and T1s and differences in TE and TM between sequences).

Fig. 2b shows diffusion-weighted spectra obtained with DDES at variable rotation angles. The oscillatory diffusion signal for the four presented rotation angles from 0 to 270° is directly evident and highlighted for the NAA peak. The highest signals are observed for a parallel and antiparallel gradient pair configuration of 0° and 180°, and the lowest for a perpendicular configuration of 90° and 270°. A high mean SNR at b =5.2 ms µm^{-2} of all rotation angles of 56.4 ± 16.6 enables a stable fitting of the nuanced sinusoidal signal modulations. The overall linewidth of (4.7 ± 0.7) Hz (average over all b-values, rotation angles, and subjects) was in line with the diffusion-time experiments.

The results from linear-combination modelling in FiTAID show only minor residuals, strongest for the major singlet peaks at the lowest b-value.

Diffusion time-dependent spectroscopy. Fig. 3 compares the currently estimated ADC(TD) and K(TD) diffusion time-dependence to results from other studies in humans and animals with our results. The mono-exponentially fitted metabolite ADCs (ADC_E) are found to be highest at the shortest TD of 6 ms ranging from 0.15 to 0.29 µm^2 ms^{-1} and plateauing for TDs ≥ 50 ms between 0.09 and 0.11 µm^2 ms^{-1} at the longest TD of 250 ms. With the exception of Glu, kurtosis increases from values between 1.0 to 1.4 at TD of 50 ms to values between 1.6 to 2.0 at TD of 250 ms (see Tab. S3 for metabolite specific ADC_E and K values). The opposing decrease found for the kurtosis of Glu at the longest diffusion time is potentially related to low SNR for the Glu signal at a TD of 250 ms at high b-values.

We used Monte Carlo (MC) simulations of 10 000 randomly initialized starting conditions, implying a two-compartment model composed of fully dispersed cylinders (astro-cylinders) and spheres to assess fitting stability. The results reveal an ill-defined problem with an *unstable* and *ambiguous* solution space. In detail, we found two possible solutions, with almost identical fitting curves: (i) a solution that contradicts realistic cell morphology with $R_c > R_s$, (ii) a solution with $R_c < R_s$ (c.f. Supporting Information Fig. S2).

Thus, in order to obtain a reasonable solution by fitting diffusion-time dependence only, it is critical to choose the initial set of fitting parameters carefully, in a physically reasonable range. We used the median values of the model parameters obtained from Monte Carlo simulations constrained to $R_c < R_s$ as an initial guess for refitting (c.f. Supporting Information Fig. S4). The estimated intrinsic diffusivities (D_0) and microstructural features (soma sizes R_s, neurites radii R_c, and cylinder fractions f_c) are reported in Tab. 1 with confidence intervals obtained from bootstrapping.

The microstructural parameters in Tab. 1 show higher levels of variation between D_0 and R_s, while R_c and f_c are consistent between metabolites. The intrinsic diffusivities D_0 are highest for NAA, Glu, mI and tCr, and lowest for tNAA and tCho, which are also the metabolites with the highest molecular weights. The radii of the spherical compartment align between NAA, tNAA, mI and tCr with an averaged value of

Table 1: **Diffusion-time experiment:** Summary of cellular microstructural features (R_s, R_c, f_c) and intrinsic diffusivities (D_0) constrained to results with $R_c < R_s$ (highlighted in yellow where fitting converged to the boundary condition $f_c \leq 0.9$). *For joint fitting of metabolite inhabiting the neuronal compartment, tNAA was fitted instead of NAAG alone due to low SNR of NAAG, and distinct differences in D_0s of NAA and tNAA.

	NAA	tNAA	Glu	NAA+tNAA*	NAA+tNAA*+Glu	tCho	mI	tCho+mI	tCr
D_0 [$\mu m^2/ms$]	0.45±0.03	0.33±0.02	0.42±0.06	0.49±0.03 0.32±0.02	0.35±0.04^{NAA} 0.24±0.02^{tNAA} 0.44±0.05^{Glu}	0.24±0.02	0.40±0.03	0.25±0.02^{tCho} 0.33±0.02^{mI}	0.44±0.04
R_s [μm]	7.4±0.7	6.2±0.7	20.4±8.5	6.6±0.5	33.4±1.2	38.3±1.5	8.5±1.7	34.9±1.8	5.9±0.9
R_c [μm]	1.5±0.2	1.2±0.2	2.5±0.5	1.3±0.1	2.1±0.1	2.4±0.3	2.0±0.2	2.4±0.1	1.3±0.2
f_c	0.82±0.04	0.82±0.02	0.90±0.07	0.83±0.02	0.90±0.03	0.86±0.05	0.89±0.04	0.90±0.03	0.82±0.04
AICc	-4.6	-3.9	-2.4	-9.1	-11.8	-3.7	-4.1	-8.6	-3.5

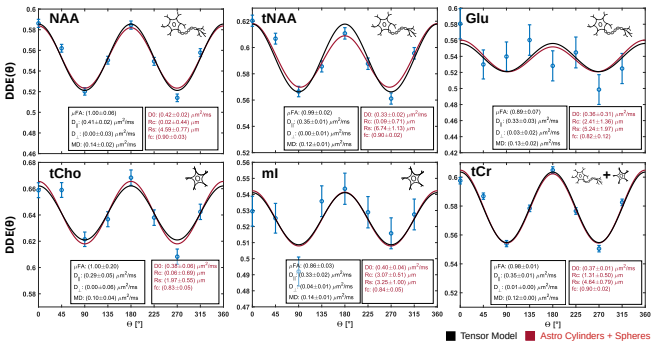

Fig. 4: **DDES fitting:** Oscillatory diffusion signal for a single subject. Two models (tissue model: astro-cylinders+spheres; tensor model) are used for fitting. Uncertainties in the plots are derived from the CRLBs. Tissue microstructural metrics are provided in the insets with standard-deviations obtained by bootstrapping.

7.0 µm and approach high values for Glu and tCho of 20.4 and 38.3 µm, respectively. Estimated cylinder radii range from 1.2 to 2.5 µm. The estimated cylinder fractions f_c are consistent among NAA, tNAA, tCho, mI and tCr with values ranging from 0.82 to 0.89, while approaching the fitting boundaries for Glu, and the jointly-fitted NAA+tNAA+Glu and tCho+mI. Although joint fitting, by combining metabolites inhabiting the same cellular confinements, lowered the Akaike Information Criterion (AICc) metric, the estimated fitting uncertainties remain unaffected. Moreover, the large soma radii R_s found for Glu and tCho translate into the joint fitting models, and add up to equally high or even higher soma radii (c.f. Tab. 1).

Double-diffusion encoded spectroscopy. Fig. 4 exemplarily shows the DDES fitting results for a single subject. The oscillatory diffusion signal DDE(Θ) is clearly visible for NAA, tNAA, tCho, and tCr, while less pronounced for Glu and mI, which also show the highest measurement uncertainties (Cramer-Rao lower bounds, CRLBs). The two fitting models, either the microstructural two-compartment model of astro-cylinders and spheres, or the representation tensor model, yield consistent results with $D_{\parallel}$ close to the estimated intrinsic diffusivity D_0 for all metabolites.

In the cohort results presented in Tab. 2, two subjects were excluded for Glu and three for mI due to poor data quality of the oscillatory signals. The cohort-wide intrinsic diffusivities D_0 and parallel diffusivities $D_{\parallel}$ are well in line with values obtained from the diffusion-time experiments constrained to $R_c < R_s$ and can potentially stabilize microstructural fitting (c.f. next section). Mean diffusivities (MD) are lower by a factor 3 to 4 , ranging from 0.10 to 0.14 $\mu m^2\, ms^{-1}$ indicating validity with a compartment in part composed of fully-dispersed cylinders(18). The radial diffusivities $D_{\perp}$ are close to zero for all metabolites, indicating a lack of sensitivity towards small neurite radii, which is probably due to coarse-graining at the rather long diffusion-time of 27.3 ms used in the DDES experiments(9). This translates into cylinder radii, R_c, that tend towards zero for most of the metabolites (except Glu and mI). In contrast, the estimated spherical radii, R_s, range from 3.3 to 6.8 µm and are consistent between metabolites, with higher values in neurons than in glia. The cylinder fractions, f_c, align between metabolites and range from 0.83 to 0.90. The microscopic fractional anisotropy, μFA, is close to 1.0 for all metabolites, indicating an anisotropic environment on the characteristic length scale of 10 µm given by the diffusion-time of this experiment and the estimated intrinsic diffusivities.

Multiparametric diffusion-time and double-diffusion modelling. The results from jointly fitting diffusion-time and double-diffusion-encoding are presented in Fig. 5. Model complexity and long computation times prevent the use of Monte Carlo simulations, and model performance was tested by choosing four initial sets from the MC simulation results as starting conditions: first the optimal solution with $R_c < R_s$ (green in Fig. S2, equal to the starting conditions used for re-fitting the diffusion-time dependence), and second three other sets of starting conditions far away from the optimal solution (details are provided in the Supporting Information in Tab. S3).

For all metabolites, the fitting converged irrespective of the

Table 2: **Cohort results of DDES experiments:** Summary of cellular microstructural features (R_s, R_c, f_c, D_0) applying a two compartment model and the diffusion metrics (μFA, $D_{\parallel}$, $D_{\perp}$, MD) applying a tensor model.

		NAA	tNAA	Glu*	tCho	mI**	tCr
Tissue Model	D0 [µm²/ms]	0.42±0.02	0.33±0.04	0.51±0.21	0.32±0.05	0.40 (/)	0.37±0.02
	Rs [µm]	6.8±1.5	6.8±1.4	4.5±1.1	5.4±2.4	3.3 (/)	6.4±1.3
	Rc [µm]	0.1±0.1	0.2±0.2	1.6±1.2	0.1±0.1	3.1 (/)	0.6±0.6
	fc	0.90±0.01	0.83±0.09	0.86±0.06	0.84±0.06	0.84 (/)	0.85±0.05
Tensor Model	µFA	1.00±0.01	0.97±0.03	0.95±0.08	0.99±0.02	0.86 (/)	0.98±0.03
	$D_{\parallel}$ [µm²/ms]	0.40±0.02	0.32±0.05	0.42±0.12	0.29±0.02	0.33 (/)	0.34±0.02
	$D_{\perp}$ [µm²/ms]	0.00±0.00	0.01±0.01	0.02±0.02	0.00±0.00	0.04 (/)	0.01±0.01
	MD [µm²/ms]	0.14±0.01	0.11±0.01	0.15±0.03	0.10±0.01	0.14 (/)	0.12±0.01

* 2 datasets for Glu; ** 1 dataset for mI (4 datasets otherwise)

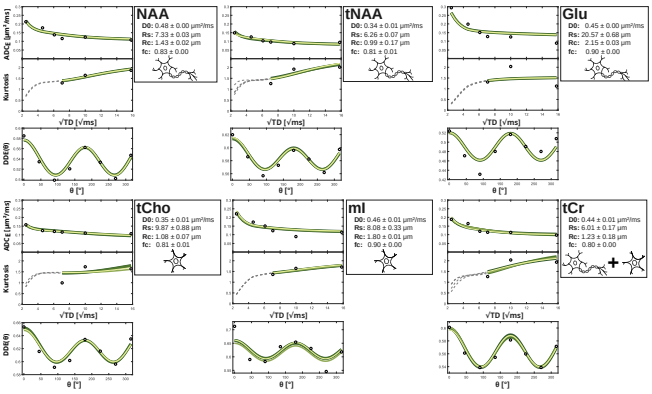

Fig. 5: **Joint fitting of TD and DDES:** Fitting used the two compartment model (astro-cylinders + spheres) and four sets of starting conditions (c.f. text). Resulting courses of $\mathrm{ADC_E(TD)}$, $\mathrm{K(TD)}$ and $\mathrm{DDE}(\Theta)$ are plotted colour coded, with dashed lines showing the back estimation of $\mathrm{K(TD)}$ towards short diffusion times. The insets provide detailed microstructural properties (D_0, R_s, R_c, f_c). Uncertainties are estimated as standard deviation of the four fitting results.

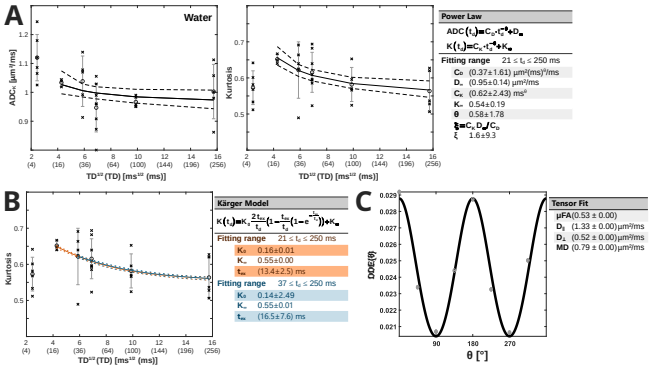

Fig. 6: **Water diffusion:** (A) Joing fitting of $\mathrm{ADC(TD)}$ and $\mathrm{K(TD)}$ employing a power-law model. (B) Fitting of K(TD) only using a Kärger exchange model restricted to TD ranges. (C) Fitting of $\mathrm{DDE}(\Theta)$ using a diffusion-tensor representation.

choice of starting values to identical biophysical solutions with $R_c < R_s$ giving largely overlapping results for $\mathrm{ADC(TD)}$, $\mathrm{K(TD)}$ and $\mathrm{DDE}(\Theta)$ and low standard deviations of the estimated microstructural properties. The highest intrinsic diffusivities D_0 were found for NAA, Glu, mI and tCr ranging from 0.44 to 0.48 $\mu m^2\,ms^{-1}$, and the lowest for tNAA and tCho of 0.34 and 0.35 $\mu m^2\,ms^{-1}$, respectively. The estimated neurite radii are close to $\approx 1\,\mu m$, with the highest value for Glu. The averaged soma radius of NAA and tNAA compartmentalized in neurons was 6.8 µm and slightly lower than the averaged value obtained from tCho and mI compartmentalized predominantly in glia of 9.0 µm. Interestingly, the initially high soma radius found for tCho in the diffusion-time experiments stabilized at a much lower value of 9.8 µm, while the large soma radius of Glu remained at 20.6 µm. The smallest soma radius was found for tCr at 6.0 µm. Cylinder fractions were equal for NAA, tNAA, tCho, and tCr, while reaching the fitting boundary for Glu and mI.

Water diffusion and exchange. Water diffusion was measured simultaneously in the diffusion-time and double-diffusion encoding experiments by applying metabolite cycling, instead of water-suppression. The results are presented in Fig. 6.

The diffusion-time dependence in Fig. 6a of $\mathrm{ADC_K(TD)}$, estimated using a Kurtosis representation, does not decay monotonically over the full TD range, though values remain highest at the shortest TD ($\mathrm{ADC_{K,6}} = 1.12 \pm 0.08$ versus $\mathrm{ADC_{K,250}} = (1.00 \pm 0.09)\,\mu m^2\,ms^{-1}$). Contrarily, kurtosis $\mathrm{K(TD)}$ is lowest at the shortest TD, peaks at $\mathrm{TD}^* = 21$ ms at 0.65 ± 0.01, and then declines towards longer TDs > 21 ms. This characteristic behaviour has been reported for water diffusion in other studies in humans and animals, indicating effects from exchange less pronounced at short TD and more dominant at long TD(29–32). The peak value at TD^* indicates the ensemble-averaged size of tissue barriers, and it may be modulated by the cell membrane permeability. Ignoring effects from permeability, i.e., assuming that the exchange time is longer than the time scale of coarse-graining suggests a typical size for the tissue restrictions on the order of $\approx 10\,\mu m$. To investigate the effect of structural disorder, a power-law was fitted jointly to $\mathrm{ADC(TD)}$ and $\mathrm{K(TD)}$ using a restricted range between $21 \leq \mathrm{TD} \leq 250$ ms to ensure model validity(33), requiring K(TD) to decay monotonically (c.f. Fig. 6)(34). Although fitting uncertainties are high, mostly driven by the variance in $\mathrm{ADC_K(TD)}$, the estimated values for Θ and ξ (dimensionless tail) are close to 0.5 and 2.0, respectively, suggesting 1D short-range structural disorder(33, 34).

In Fig. 6b a Kärger exchange model was fitted to K(TD) first in the range between $21 \leq \mathrm{TD} \leq 250$ ms and second in the range between $37 \leq \mathrm{TD} \leq 250$ ms where the power law fitting suggests a minimal to absent $\mathrm{ADC_K(TD)}$ dependence. The estimated exchange times t_{ex} of 13.4 and 16.5 ms are well in line with TD^* of the maximum kurtosis at 21 ms and previous works(35–37) (note: the TD range ≤ 21 ms needs to be sampled with more TD points to determine the kurtosis peak accurately(29)).

The oscillatory signal obtained in the DDE experiments is presented in Fig. 6c and fitted using a tensor model. The overall data quality of the water signal aligns very well with the fitting result, and uncertainties are small. The estimated mean-diffusivity, MD, is lower than ADCs obtained in the diffusion time experiments, indicating diffusion-filtering effects due to higher b-values of b =5.2 ms μm^{-2} used for DDE, suppressing signal from the faster diffusion pole in the less restricted extracellular compartment.

Discussion

To date, the standard model of diffusion MR spectroscopy consists of fully dispersed cylinders only, representing neurites. However, even this simplified model requires ultra-high b-values > 10 ms μm^{-2} to be acquired in order to fit data consistently(18). The presented work successfully demonstrates another approach using multi-parametric dMRS in the human brain, by combining diffusion-time and double-diffusion encoding spectroscopy to probe cellular microstructure. Our findings reveal a clear dependence of metabolite ADC and K on the diffusion time, show that DDES provides complementary information, and demonstrate that joint modelling of both techniques allows the standard model to be

extended by a second compartment of spheres representing cellular soma. We provide evidence that multi-parametric diffusion MRS largely stabilizes fitting and removes ambiguous unphysical solutions.

Metabolite diffusion. The diffusion-time dependence is consistent with the presence of restricting barriers, such as cell membranes and organelles that hinder molecular motion more at longer time scales. Determined ADC(TD) and K(TD) agree well with previous studies (c.f. Fig. 3). At short TDs (< 25 ms), metabolites probe the intracellular environment over short distances, resulting in higher ADCs and lower Kurtosis, more sensitive to factors like cytoplasmic viscosity and molecular crowding. As TD increases further, metabolites have a higher probability of interacting with cellular boundaries, leading to a reduction in ADC and an increase in Kurtosis to characteristic plateaus. This plateau is three to four times lower for ADC(TD) than the estimated intrinsic diffusivity D_0. For neuronal markers (tNAA, Glu) it remained slightly below values from studies in other primates, while for glial markers (tCho, mI) it confirms results obtained in other primates, and it turned out higher than in rodents. Although this might indicate differences in neural spine density between humans and primates, it is worth noting that our results for NAA's TD dependence only (i.e., without NAAG) yield a similar high long time ADC plateau and future studies are needed to investigate NAA and tNAA diffusion more rigorously. Contrarily, our results for glial markers confirm previous works showing differences between humans/primates and rodents with higher cellular complexity found in the former group(38, 39). The observed increase in K(TD) further supports the notion of increasing restriction effects at longer time scales elevating the non-Gaussian nature of metabolite diffusion in complex and heterogeneous intracellular environments.

By using Monte-Carlo simulations in the diffusion-time experiments, we found a degenerated solution space giving two distinct solutions: (i) contradicting expected cellular morphologies with $R_s < R_c$, and (ii) in line with $R_c < R_s$. However, both solutions have almost identical fitting curves in the measured TD ranges, responsible for model ambiguity and unstable fitting. Comparing the back-estimation of K(TD) towards diffusion-times < 50 ms, one notices differences, where solutions with $R_s < R_c$ show a steady K(TD) decay. Thus, in future experiments, it might be possible to stabilize fitting by measuring K(TD) in the short diffusion-time range, which was not possible in our experiments because of PNS limitations.

In order to still derive microstructural features from diffusion-time dependence fitting only, we had to constrain the solution space to $R_c < R_s$ and select starting conditions carefully from Monte Carlo simulations, yielding: (i) soma radii R_s ranging from 7.4 to 20.4 μm for neural markers (NAA, tNAA and Glu [highest value]) and of 8.5 to 38.3 μm for glial markers (tCho [highest value] and mI), (ii) neurite radii R_c consistent between cellular compartments with slightly lower values in neurons (average: 1.7 μm) than in glia (average: 2.2 μm), (iii) cylinder fractions f_c between 82 to 90 % (fitting boundaries imposed for $f_c \leq 90$ %). Moreover, we investigated joint modelling of metabolites inhabiting the same cellular compartments, by allowing each metabolite to diffuse individually (metabolite specific D_0s), but constraining cell-type specific parameters (R_s, R_c, f_c) to equal values. Though estimated AICc values are lower than for individual metabolite modelling, solutions remained unstable and ambiguous.

To study if double-diffusion encoded spectroscopy can provide complementary information to stabilize microstructural modelling and restrict the solution space, additional experiments were conducted. The resulting intrinsic diffusivities D_0 accurately reproduce the results obtained from the diffusion-time experiments in the solution space with $R_c < R_s$. This, in consequence, hints that incorporating both datasets – diffusion-time dependence and double-diffusion encoding – into a joint model can restrict the solution space to results with $R_c < R_s$. However, we also found that double-diffusion encoding alone cannot provide accurate microstructural properties. Yet, soma radii R_s remained consistent between metabolites, with higher values in neurons (neuron: 6.8, glia: 3.3 μm), overall R_s values remain considerably lower than in the diffusion-time experiments. Moreover, neurite radii R_c converge towards zero for most of the metabolites (c.f. Tab. 2). The reason for this discrepancy might originate from the rather long diffusion-time of 27.3 ms at which DDES experiments were conducted and a resulting lack of microstructural sensitivity towards small cellular structures due to coarse-graining(9). A possible solution might be to also acquire DDES at multiple diffusion-times including the short TD range < 10 ms, which was not possible in our experiments due to limitations in the maximum gradient amplitudes.

To still resolve this problem, we implemented a joint model combining both experiments. To test model stability, we initialized the joint fitting firstly at the optimal solution derived from the diffusion-time dependence results constrained to $R_c < R_s$, and secondly at three other starting conditions far away from the optimal solution, including the results contradicting realistic morphologies with $R_c > R_s$. Irrespective of the choice of starting conditions, fitting converged stably towards almost identical solutions consistent with $R_c < R_s$ (c.f. Fig. 5). The obtained K(TD) dependence back estimated towards short diffusion-times confirms the results from the diffusion-time fitting constrained to $R_c < R_s$ with their characteristic K(TD) dependences. The estimated microstructural properties and intrinsic diffusivities were consistent between all metabolites (except for Glu, where the large soma radius remained at 20.6 µm). Excluding Glu, we obtained soma radii slightly lower in neurons of 6.8 µm than in glia of 9.0 µm, while neurite radii remained similar in both compartments with an average value of 1.3 µm.

Overall, our results suggest: (i) that the diffusion-time dependence of brain metabolites can readily be measured in humans, (ii) that double-diffusion encoding spectroscopy extends the parameter space providing complementary information, (iii) that joint modelling allows stabilizing microstructural modelling and extending the standard model by a second compartment.

Moreover, this approach shows promise not only to be applicable on prototype MR scanners with strong gradients, but also in clinical settings, as we have shown before that short diffusion-times of ≈ 6 ms are accessible on clinical PRISMA scanners(28).
In order to further extend the standard model of dMRS, a promising approach is to increase diffusion-times beyond 500 ms, which might enable the estimation of the cylinder length as a measure for the axial dimensions of neurites(6, 10, 39).

Water diffusion. We demonstrate that metabolite cycling in dMRS cannot only be a valuable approach to compensate for motion(28), but also provides additional microstructural information on water exchange and structural disorder measured simultaneously in the same voxel.
Diffusion-time dependence of water's ADC(TD) and K(TD) fitted using a power-law suggests 1D short-range structural disorder, confirmed in other studies in gray matter rich brain regions(33, 34). In particular, K(TD) does not increase monotonically with TD and, instead, peaks at 21 ms, followed by a further decline. This directly confirms effects from water exchange. We used a Kärger exchange model revealing exchange times between 13.4 to 16.5 ms supported by other dMRI studies(35–37).
This is further confirmed by the oscillatory DDE water signal, resulting in a lower μFA of water of 0.53 than for metabolites (≈ 1.00). This indicates that water diffusion is multi-compartmental and most likely affected by exchange between compartments. Moreover, differences found in mean diffusivity (MD) of double-diffusion encoding compared with the ADCs of the diffusion-time experiment might originate from filtering effects, where less restricted compartments contribute to a lesser extent to the overall diffusion signal at higher b-values.

Limitations. Some noteworthy limitations of this study are:

- Although other studies have shown little to no effects from compartment specific T2s in the echo-time ranges used in our experiments(8, 16, 18, 40, 41), we cannot fully exclude potential filtering effects, where restricted compartments with shorter T2 become less visible at longer TE as used with semiLaser.
- Even though we maximized the gray matter fractions during voxel positioning in the PCC, we cannot exclude a remaining preferential fibre direction orientation which can originate in slightly anisotropic diffusion directionality. This in particular might affect the diffusion-time experiments, where no isotropic encoding could be achieved due to gradient limitations on the Connectom-A scanner. Although, we think that this effect is negligible in our cohort results, future experiments should implement multi-directional diffusion encoding for the diffusion-time dependent measurements.
- Although uncertainties for the fitting of the water signal appear low, we found that even small changes in the data quality (e.g., not applying outlier detection) have a strong effect on the estimated t_{ex}, and more diffusion-times between 21 and 250 ms are required in future experiments to estimate exchange rates accurately.

Conclusion

Morphologic changes in the cellular structure of neurons and glia are a precursor in many neurodegenerative pathologies(42–45), and it has become increasingly important to establish non-invasive techniques that can provide detailed microstructural information, at best with cellular specificity.
In this work, we present for the first time multi-parametric dMRS in humans as a possible solution and as a logical extension to conventional dMRS to improve microstructural specificity and sensitivity. The combination of diffusion-time and double-diffusion encoding enables a second compartment, representing cellular soma, to be included in the standard tissue model of dMRS and largely stabilizes cellular modelling. This, in combination with the cellular specificity of dMRS, can provide very valuable information in cases where detailed cellular morphology can potentially serve as a biomarker. For instance, it is well reported that microglial (macrophages of the neuroimmune system) and astrocytes (homeostatic balance) change shape and size dramatically in response to immune challenges. These changes cover a wide spectrum from ramified (resting-state), to hypertrophic (reactive), to amoeboid (phagocytic) cell shapes, where each indicates a specific stage in the neuroimmune pathway. By potentially disentangling changes between soma shape and process complexity, a better disease phenotyping can be achieved, e.g., in Alzheimer's disease(45, 46).
On prototype MR scanners with ultra-strong gradients, either sampling the diffusion-time dependence of the Kurtosis K(TD) or the double diffusion-encoding signal at shorter diffusion-times < 10 ms may allow to resolve model ambiguities as well.
As this is not feasible on clinical MR scanners, our multi-parametric strategy –combining diffusion-time dependence and double-diffusion encoding– remains a potential solution to make quantitative dMRS available for diagnostics in clinical settings. However, to apply this protocol in individual subjects or patients, it needs refinement to reduce measurement time. One has to carefully select the needed diffusion-times and rotation-angles, to obtain the right amount of microstructural information while still preserving enough signal-to-noise ratio. A potential protocol might consist of three diffusion-times of 6, 25 and 100 ms, combined with four rotation angles for DDES of 0, 90, 180 and 270° and should allow acquisition times well below 1 h.

Materials and Methods

Voxel positioning and tissue segmentation used 1 mm^3 isotropic MPRAGE images (TE/TI/TR: 2/ 857/ 2300 ms, flip angle: 9°). Shimming was performed using product automatic second order GRE double acquisition (Siemens, Erlangen, Germany).

Diffusion time experiments. Measurements were conducted on a 3 T Connectom-A MR scanner (Siemens Healthineers, Erlangen, Germany) using a 32-channel receive head-coil. Brain metabolite diffusion was measured at (i) short to intermediate TDs (6, 21, 37 ms) using semiLASER (b_{max} = 3 ms µm^{-2}, G_{max} = 254 mT m^{-1})(28), and (ii) intermediate to long TDs (50, 100, 250 ms) with STEAM (b_{max} = 8 ms µm^{-2}, G_{max} = 151 mT m^{-1})(47) (detailed settings are provided in the Supporting Information in Tab. S2). Diffusion gradients had bipolar sinusoidal shape at the shortest TD and trapezoidal shapes otherwise(11, 28). For STEAM six outer-volume-suppression (OVS) bands were placed around the volume of interest (VOI) to improve localization and prevent lipid contamination and spurious echoes. The diffusion encoding direction was chosen along the x/y diagonal with identical gradient amplitudes to achieve sufficiently high b-values, but not along z to minimize table vibrations. For $b \leq 3$ ms µm^{-2} 32 transients were acquired and 64 otherwise. Fluid-attenuated inversion recovery (FLAIR) was used to suppress cerebrospinal fluid (CSF) and metabolite cycling (MetCyl) to measure water and metabolite diffusion simultaneously. Cross-terms were compensated by diffusion-gradient polarity inversion in successive transients. A macromolecular baseline (MMBG) was acquired for all TDs for STEAM using metabolite nulling (inversion time: 765 ms) and moderate diffusion-weighting (5 ms µm^{-2}). A macromolecular baseline model composed of 80 Voigt-lines was applied for MMBG parametrization and smoothing(48). The remaining Cr_{CH2} moiety was removed by modelling and subtracting a single Voigt-line with a T2 of 125 ms at 4.0 ppm.

Ten healthy subjects ((32.8±3.4) ; 7 female) were recruited in agreement with approval from the Cardiff University School of Psychology ethics review board. Subjects were screened for potential MR risk factors and gave their informed consent. The VOI ((10.0 ± 1.5) mL) was placed midline in the posterior cingulate cortex (PCC) and gray matter fraction was maximized with an average of (70.9 ± 1.7) % taking care of preventing contamination from subcutaneous fat and CSF. The number of measurements per TD is given as {TD[ms],measurement numbers} and were {6,6}, {21,3}, {37,7}, {50,8}, {100,7} and {250,8}.

Double-diffusion encoded experiments. Measurements were conducted on two sites on 3T Siemens PRISMA MR scanners (Siemens Healthineers, Erlangen, Germany) using 32-channel receive head-coils. Non-water suppressed diffusion-weighted spectra were acquired using the same semiLASER sequence as applied for the diffusion-time experiments(28). The crushing scheme was optimized to reduce spurious diffusion-weighting by splitting crushing gradients to null zero-order moments in-between the RF pulses (Fig. 1b). Diffusion-weighting was applied at a b-value of 5.2 ms µm^{-2} with DDE encoding along three orthogonal planes ([1.0 1.0 -0.5], [-0.5 1.0 1.0], [1.0 -0.5 1.0]) using an 8-step rotation-cycle (0, 45, ..., 315°). Interleaved within the rotation-cycle, 3 × 16 transients were acquired at $b = 0$. For each rotation-angle, data with positive and negative gradient polarity were acquired with 24 transients each (144 per angle). The total measurement time per subject was 1 h10 min (detained sequence settings can be found in Tab. S2).

Data were obtained from four healthy subjects ((56.7 ± 14.4) yrs all male), with the VOI ((16.1 ± 2.4) mL) located in the PCC (GM: (63.0 ± 5.4) %). Subject recruitment was done in agreement with the local ethics review board.

Data processing. Single transients were stored in raw twix format without coil-channel averaging or preprocessing. A self-developed MatLab pipeline (MathWorks) was used for coil-channel combination, phase-offset, frequency-drift and eddy-current correction and motion compensation relying on the inherent water reference(26, 49).

Spectral Fitting. Individual metabolite basis-sets were simulated in MARSS accounting for sequence type (spin-/stimulated echo), sequence timings (TE and TM), and RF pulse profiles(50). The basis-sets of 18 metabolites [aspartate (Asp), gamma-aminobutyric acid (GABA), glucose (Glc), glutamine (Gln), glutamate (Glu), glycine (Gly), glutathione (GSH), lactate (Lac), myo-inositol (mI), N-acetylaspartate (NAA), N-acetylaspartylglutamate (NAAG), phosphorylethanolamine (PE), scyllo-inositol (sI), taurine (Tau), total choline [tCho = glyceryl phosphoryl choline (GPC) + phosphocholine (PCho)], total creatine [tCr = creatine (Cr) + phosphocreatine (PCr)])] were included in the fitting model. To address differences in the T2s of metabolite moieties a relative Lorentz broadening of 0.15 Hz was applied to NAA_{asp}, of 0.50 Hz to $NAAG_{asp}$ and $NAAG_{glu}$, of 0.70 Hz to the Cr_{CH2} and PCr_{CH2} singlets, of 0.20 Hz to the PCho and GPC singlets, and of 0.20 Hz to the GSH singlet(51). For STEAM, the parametrized MMBG patterns were added to the fitting model at each TM(48).

Spectral fitting was performed sequentially by linear-combination modelling in FiTAID using Levenberg-Marquardt χ^2-minimization in the frequency domain restricted to 0.0 to 4.2 ppm(52, 53). Metabolites within the groups [Asp, NAAG, PE, tCr], [Glc, mI, sI], [Gln, Glu] and [Gly, GSH] were constrained to equal Lorentzian broadening, while frequency-offset, zero-order phase and Gaussian broadening were equal for all of them. The corrected b-values were derived from the sequence chronograms, taking crusher and slice selection gradients into account.

Multiparametric tissue modelling of metabolite diffusion. Tissue models were implemented in MatLab using an analytical solution for PG and OG encoding(54–56), and the matrix formalism (MISST toolbox) for DDE encoding(57–61). A two-compartment model composed of fully dispersed cylinders (astro-cylinders) and spheres was implemented for fitting the diffusion-time dependences, double-diffusion encoding and both datasets jointly. The model parameters are D_0 (intrinsic free diffusivity), R_c (radius of the cylinder compartment reflecting cellular neurite radii), R_s (radius of the spherical compartment reflecting cellular soma size), and f_c (fraction of the cylinder compartment with $1-f_c = f_s$ [fraction of spheres]).

For the diffusion-time experiments, the metabolite areas and their Cramér-Rao lower bounds (CRLBs), applied as inverse weights, served to inform two diffusion representations implemented in MatLab: (i) mono-exponential fitting of $ADC_E(TD)$ alone at low b-values ($\leq 3\,\mu m^2\,ms^{-1}$) for semi-LASER and STEAM, and (ii) fitting of a kurtosis representation with $ADC_K(TD)$ and K(TD) for the STEAM acquisitions only over the full b-value range. Moreover, fitting included an outlier detection to remove spectra potentially affected by motion by either include all b-values or iteratively removing a single b-value from the fitting and identifying the fit with the lowest Akaike Information Criterion (AICc). For microstructural modelling, only the diffusion-time dependence of $ADC_E(TD)$ and K(TD) was used.

For fitting the tissue model to $ADC_E(TD)$ and K(TD), the signal for a specific configuration (D_0, R_s, R_c, f_c) was simulated for the TD configuration used and up to $b_{max} = 8\,ms\,\mu m^{-2}$ using the same b-values as applied in the STEAM experiments. The model specific mono-exponential ADC_E and kurtosis K were estimated by least-squares optimization up to $b_{max} = 3\,ms\,\mu m^{-2}$ and $b_{max} = 8\,ms\,\mu m^{-2}$, respectively, giving the model functions as $ADC_E(D_0, R_s, R_c, f_c, TD, b)$ and $K(D_0, R_s, R_c, f_c, TD, b)$.

These model functions were then used for fitting the measured diffusion-time dependence of $ADC_E(TD)$ and Kurtosis K(TD) simultaneously with boundary conditions implied on $0.40 \leq f_c \leq 0.90$ using MatLab's trust region reflective algorithm. Starting values were estimated beforehand by Monte Carlo simulations by fitting 10 000 uniformly distributed starting parameter realizations between $0.00 \leq D_0 \leq 0.50\,\mu m^2\,ms^{-1}$, $0 \leq R_c \leq 15\,\mu m$, $0 \leq R_s \leq 40\,\mu m$ and $0.40 \leq f_C \leq 0.90$. The median of the 10 % quantile of these fits with the lowest root-mean-square-errors (RMSE) and constraint to $R_c < R_s$ was used as starting values for refitting the diffusion-time dependence. The fitting uncertainties were estimated by residual bootstrapping using 250 random noise realizations.

Moreover, we investigated if a joint modelling approach of the diffusion time dependence of metabolites inhabiting the same cellular compartments can improve fitting stability. For this purpose D_0 values were set metabolite-specifically at global Rs, Rc and fc values, giving $ADC_E(D_{0,i}, R_s, R_c, f_c, TD, b)$ and $K(D_{0,i}, R_s, R_c, f_c, TD, b)$, with *i* the index of the metabolites.

The double-diffusion encoding experiment used a tissue model implemented in the MISST toolbox accounting for all rotation angle configurations giving $DDE(D_0, R_s, R_c, f_c, \Theta, b)$ and in addition a signal representation fitting the powder average of 256 uniformly oriented diffusion-tensors giving $DDE(D_\parallel, D_\perp, \Theta, b)$. The estimate radial ($D_\parallel$) and axial ($D_\perp$) diffusion-components were used to calculate the mean diffusivity (MD) and microscopic fractional anisotropy (μFA)(62).

Last but not least a joint fitting model was implemented combining $ADC_E(D_0, R_s, R_c, f_c, TD, b)$, $K(D_0, R_s, R_c, f_c, TD, b)$ and $DDE(D_0, R_s, R_c, f_c, \Theta, b)$ to study potential improvements by implying a multi-parametric dataset composed of diffusion-time dependence and double-diffusion encoding experiments.

Modelling of water diffusion. Water was acquired simultaneously with the same sequence settings in both experiments by metabolite cycling. The diffusion-time experiment used a kurtosis representation of ($ADC_{K,H2O}(TD)$ and $K_{H2O}(TD)$) implemented in MatLab modelling the b-values $\leq 3\,\mu m^2\,ms^{-1}$ for both semiLASER and STEAM acquisitions. Then, we used a power law representation to fit diffusion-time dependences of water's ADC(TD) and K(TD), and a Kärger model to fit K(TD) alone, to estimate structural disorder and exchange rates. Moreover, we used a diffusion-tensor model to fit water's $DDE(\Theta)$ to estimate the μFA, $D_\parallel$, and $D_\perp$.

Sequence validation. The sequences were validated in two phantom measurements at room temperature (20.5 ± 0.7) °C. A detailed analysis is reported in the Supporting Information in Fig. S1.

First, in a water phantom from the National Institute of Standards and Technology (NIST) containing a 40 % mass fraction of polyvinylpyrrolidone (PVP) to slow diffusion. This experiment aimed to exclude bias related to different diffusion-encoding strategies (OG vs. PG) and diffusion times (TD). All settings were equally adjusted to the *in vivo* condition and free water diffusion coefficients estimated by mono-exponential fitting.

Second, measurements were conducted in a "braino" phantom (GE medical systems) to measure metabolite diffusion and exclude bias introduced by differences in the basis-sets and due to J-evolution when TE, mixing time (TM), echo types (spin vs stimulated echo) or diffusion-encoding (OG vs. PG vs. DDE) vary. Due to fast metabolite diffusion, the b-value range was reduced to 8 linearly spaced values from 0.1 to $1.5\,ms\,\mu m^{-2}$. Diffusion weighted spectra of myo-inositol (mI, 5.0 mM), N-acetylaspartate (NAA, 12.5 mM), glutamate (Glu, 12.5 mM), creatine (Cr, 10.0 mM), lactate (Lac, 5.0 mM), and choline (Cho, 3.0 mM) were fitted sequentially in FiTAID. Metabolite pattern amplitudes were used to inform a mono-exponential free diffusion model and a diffusion-tensor representation implemented in MatLab to estimate individual metabolite diffusivities.

The signal attenuation in the NIST phantom for the diffusion-time experiments is mono-exponential and the estimated free diffusion constants, along with their 95 % confidence intervals (CI), are consistent - irrespective of sequence-type, echo-time or diffusion-encoding (c.f. Fig. S1A). The averaged diffusivity of water was $(0.56 \pm 0.02)\,\mu m^2\,ms^{-1}$. Different offsets in the diffusion decay signals originate from T1 and T2 relaxation at different echo- and mixing-times (a detailed analysis can be found in the Supporting Information).

Likewise, free metabolite diffusion measured in a braino phantom yields equal metabolite diffusivities independent of echo-, mixing- or diffusion-times for NAA (0.57 ± 0.04), tCr (0.74 ± 0.04), Cho (0.84 ± 0.04), Lac (0.81 ± 0.04), Glu (0.64 ± 0.06) and mI (0.58 ± 0.15) $\mu m^2\,ms^{-1}$. The spectral quality reported in Fig. S1B at the shortest (semiLASER) and longest (STEAM) TDs allows all included metabolites to be identified visually and demonstrates the effects from J-evolution by an out of phase signal of Lac, Glu and mI

at the longest TE for semiLASER. A power-law model (c.f. Fig. S1C) yields a significant ($p < 0.01$) inverse relation between molecular weight and free diffusivity, giving an exponent α of 0.58 ± 0.09, well in line with other studies(63). Validation of DDES in the braino phantom yields an expected microscopic fractional anisotropy (μFA) of zero for all metabolites and diffusion equal for $D_{\parallel}$ and $D_{\perp}$ independent of encoding direction. The resulting mean diffusivities (MDs) align well with the diffusivities obtained from the diffusion-time experiments (except for slightly higher free diffusivities of myo-inositol) (c.f. Fig. S1D).

ACKNOWLEDGEMENTS

AD is supported by a Swiss National Science Foundation Fellowship (SNSF #202962). MA is supported by a Wellcome Trust Investigator Award (219536/Z/19/Z). MP is supported by a UKRI Future Leaders Fellowship (MR/T020296/2 and 1073) and the MRC Research Grant MR/W031566/1. KŞ is supported by a UKRI Future Leaders Fellowship (MR/T020296/2). DKJ is supported by a Wellcome Trust Strategic Award (104943/Z/14/Z) and the MRC Research Grant MR/W031566/1.

Bibliography

1. Klaas Nicolay, Kees P. J. Braun, Robin A De Graaf, Rick M Dijkhuizen, Marijn J Kruiskamp, Robin A. de Graaf, Rick M Dijkhuizen, and Marijn J Kruiskamp. Diffusion NMR spectroscopy. *NMR in Biomedicine*, 14(2):94–111, apr 2001. ISSN 09523480. doi: 10.1002/nbm.686.
2. Itamar Ronen and Julien Valette. Diffusion-Weighted Magnetic Resonance Spectroscopy. In *eMagRes*, volume 4, pages 733–750. John Wiley & Sons, Ltd, Chichester, UK, dec 2015. ISBN 9780470034590. doi: 10.1002/9780470034590.emrstm1471.
3. Peng Cao and Ed X. Wu. In vivo diffusion MRS investigation of non-water molecules in biological tissues. *NMR in Biomedicine*, 30(3):e3481, mar 2017. ISSN 09523480. doi: 10.1002/nbm.3481.
4. Marco Palombo, Noam Shemesh, Itamar Ronen, and Julien Valette. Insights into brain microstructure from in vivo DW-MRS. *NeuroImage*, (June):1–20, nov 2017. ISSN 10538119. doi: 10.1016/j.neuroimage.2017.11.028.
5. Ji-Kyung Choi, Alpaslan Dedeoglu, and Bruce G. Jenkins. Application of MRS to mouse models of neurodegenerative illness. *NMR in Biomedicine*, 20(3):216–237, may 2007. ISSN 09523480. doi: 10.1002/nbm.1145.
6. Julien Valette, Clémence Ligneul, Charlotte Marchadour, Chloé Najac, and Marco Palombo. Brain Metabolite Diffusion from Ultra-Short to Ultra-Long Time Scales: What Do We Learn, Where Should We Go? *Frontiers in Neuroscience*, 12(JAN):1–6, jan 2018. ISSN 1662-453X. doi: 10.3389/fnins.2018.00002.
7. Christopher D. Kroenke, Joseph J.H. H Ackerman, and Dmitriy A. Yablonskiy. On the nature of the NAA diffusion attenuated MR signal in the central nervous system. *Magnetic Resonance in Medicine*, 52(5):1052–1059, nov 2004. ISSN 07403194. doi: 10.1002/mrm.20260.
8. Chloé Najac, Francesca Branzoli, Itamar Ronen, and Julien Valette. Brain intracellular metabolites are freely diffusing along cell fibers in grey and white matter, as measured by diffusion-weighted MR spectroscopy in the human brain at 7 T. *Brain Structure and Function*, 221(3):1245–1254, apr 2016. ISSN 1863-2653. doi: 10.1007/s00429-014-0968-5.
9. Dmitry S. Novikov, Els Fieremans, Sune N. Jespersen, and Valerij G. Kiselev. Quantifying brain microstructure with diffusion MRI: Theory and parameter estimation. *NMR in Biomedicine*, (October 2016):1–53, 2018. ISSN 10991492. doi: 10.1002/nbm.3998.
10. Charlotte Marchadour, Emmanuel Brouillet, Philippe Hantraye, Vincent Lebon, and Julien Valette. Anomalous diffusion of brain metabolites evidenced by diffusion-weighted magnetic resonance spectroscopy in vivo. *Journal of Cerebral Blood Flow and Metabolism*, 32(12): 2153–2160, dec 2012. ISSN 0271-678X. doi: 10.1038/jcbfm.2012.119.
11. Clémence Ligneul and Julien Valette. Probing metabolite diffusion at ultra-short time scales in the mouse brain using optimized oscillating gradients and "short"-echo-time diffusion-weighted MRS. *NMR in biomedicine*, 30(1):e3671, jan 2017. ISSN 1099-1492. doi: 10.1002/nbm.3671.
12. Jens H. Jensen, Joseph A. Helpern, Anita Ramani, Hanzhang Lu, and Kyle Kaczynski. Diffusional kurtosis imaging: The quantification of non-gaussian water diffusion by means of magnetic resonance imaging. *Magnetic Resonance in Medicine*, 53(6):1432–1440, jun 2005. ISSN 0740-3194. doi: 10.1002/mrm.20508.
13. Marco Palombo, Clémence Ligneul, Chloé Najac, Juliette Le Douce, Julien Flament, Carole Escartin, Philippe Hantraye, Emmanuel Brouillet, Gilles Bonvento, and Julien Valette. New paradigm to assess brain cell morphology by diffusion-weighted MR spectroscopy in vivo. *Proceedings of the National Academy of Sciences*, 113(24):6671–6676, 2016. ISSN 0027-8424. doi: 10.1073/pnas.1504327113.
14. Marco Palombo, Clemence Ligneul, Edwin Hernandez-Garzon, and Julien Valette. Can we detect the effect of spines and leaflets on the diffusion of brain intracellular metabolites? *NeuroImage*, 182(May 2017):283–293, 2018. ISSN 10959572. doi: 10.1016/j.neuroimage.2017.05.003.
15. Marco Palombo, Daniel C Alexander, and Hui Zhang. A generative model of realistic brain cells with application to numerical simulation of the diffusion-weighted MR signal. *NeuroImage*, 188(November 2018):391–402, mar 2019. ISSN 10538119. doi: 10.1016/j.neuroimage.2018.12.025.
16. Eloïse Mougel, Julien Valette, and Marco Palombo. Investigating exchange, structural disorder and restriction in Gray Matter via water and metabolites diffusivity and kurtosis time-dependence. *Intl. Soc. Mag. Reson. Med.*, page 255, jun 2023. doi: 10.48550/arXiv.2306.16984.
17. Rafael N Henriques, Marco Palombo, Sune N Jespersen, Noam Shemesh, Henrik Lundell, and Andrada Ianuş. Double diffusion encoding and applications for biomedical imaging. *Journal of Neuroscience Methods*, (July):108989, nov 2020. ISSN 01650270. doi: 10.1016/j.jneumeth.2020.108989.
18. Clémence Ligneul, Chloé Najac, André Döring, Christian Beaulieu, Francesca Branzoli, William T Clarke, Cristina Cudalbu, Guglielmo Genovese, Saad Jbabdi, Ileana Jelescu, et al. Diffusion-weighted mr spectroscopy: consensus, recommendations and resources from acquisition to modelling. *arXiv preprint arXiv:2305.10829*, 2023.
19. J Pfeuffer, I Tkac, and R Gruetter. Extracellular-intracellular distribution of glucose and lactate in the rat brain assessed noninvasively by diffusion-weighted 1H nuclear magnetic resonance spectroscopy in vivo. *Journal of Cerebral Blood Flow and Metabolism*, 20(4): 736–746, apr 2000.
20. Jacob Ellegood, Chris C Hanstock, and Christian Beaulieu. Trace apparent diffusion coefficients of metabolites in human brain using diffusion weighted magnetic resonance spectroscopy. *Magnetic resonance in medicine : official journal of the Society of Magnetic Resonance in Medicine / Society of Magnetic Resonance in Medicine*, 53(5):1025–32, may 2005. ISSN 0740-3194. doi: 10.1002/mrm.20427.
21. Julien Valette, Martine Guillermier, Laurent Besret, Philippe Hantraye, Gilles Bloch, and Vincent Lebon. Isoflurane strongly affects the diffusion of intracellular metabolites, as shown by 1H nuclear magnetic resonance spectroscopy of the monkey brain. *Journal of Cerebral Blood Flow & Metabolism*, 27(3):588–596, mar 2007. ISSN 0271-678X. doi: 10.1038/sj.jcbfm.9600353.
22. Hermien E. Kan, Aranee Techawiboonwong, Matthias J. P. van Osch, Maarten J. Versluis, Dinesh K. Deelchand, Pierre-Gilles G Henry, Małgorzata Marjańska, Mark A. van Buchem, Andrew G. Webb, Itamar Ronen, M Marjanska, Mark A. van Buchem, Andrew G. Webb, and Itamar Ronen. Differences in apparent diffusion coefficients of brain metabolites between grey and white matter in the human brain measured at 7 T. *Magnetic Resonance in Medicine*, 67(5):1203–1209, may 2012. ISSN 07403194. doi: 10.1002/mrm.23129.
23. Chloé Najac, Charlotte Marchadour, Martine Guillermier, Diane Houitte, Velislav Slavov, Emmanuel Brouillet, Philippe Hantraye, Vincent Lebon, and Julien Valette. Intracellular metabolites in the primate brain are primarily localized in long fibers rather than in cell bodies, as shown by diffusion-weighted magnetic resonance spectroscopy. *NeuroImage*, 90:374–380, apr 2014. ISSN 10538119. doi: 10.1016/j.neuroimage.2013.12.045.
24. Ayse Ece Ercan, Aranee Techawiboonwong, Maarten J. Versluis, Andrew G. Webb, and Itamar Ronen. Diffusion-weighted chemical shift imaging of human brain metabolites at 7T. *Magnetic Resonance in Medicine*, 73(6):2053–2061, 2015. ISSN 15222594. doi: 10.1002/mrm.25346.
25. Dinesh K. Deelchand, Edward J. Auerbach, and Małgorzata Marjańska. Apparent diffusion coefficients of the five major metabolites measured in the human brain in vivo at 3T. *Magnetic Resonance in Medicine*, 79(6):2896–2901, jun 2018. ISSN 07403194. doi: 10.1002/mrm.26969.
26. André Döring, Victor Adalid, Chris Boesch, and Roland Kreis. Diffusion-weighted magnetic resonance spectroscopy boosted by simultaneously acquired water reference signals. *Magnetic Resonance in Medicine*, 80(6):2326–2338, dec 2018. ISSN 15222594. doi: 10.1002/mrm.27222.
27. Carson Ingo, Wyger Brink, Ece Ercan, Andrew G. Webb, and Itamar Ronen. Studying neurons and glia non-invasively via anomalous subdiffusion of intracellular metabolites. *Brain Structure and Function*, 223(8):3841–3854, 2018. ISSN 18632661. doi: 10.1007/s00429-018-1719-9.
28. André Döring and Roland Kreis. Magnetic resonance spectroscopy extended by oscillating diffusion gradients: Cell-specific anomalous diffusion as a probe for tissue microstructure in human brain. *NeuroImage*, 202(August):116075, aug 2019. ISSN 1053-8119. doi: 10.1016/j.neuroimage.2019.116075.
29. Nadya Pyatigorskaya, Denis Le Bihan, Olivier Reynaud, and Luisa Ciobanu. Relationship between the diffusion time and the diffusion MRI signal observed at 17.2 tesla in the healthy rat brain cortex. *Magnetic Resonance in Medicine*, 72(2):492–500, aug 2014. ISSN 0740-3194. doi: 10.1002/mrm.24921.
30. Manisha Aggarwal, Matthew D. Smith, and Peter A. Calabresi. Diffusion-time dependence of diffusional kurtosis in the mouse brain. *Magnetic Resonance in Medicine*, 84(3):1564–1578, 2020. ISSN 15222594. doi: 10.1002/mrm.28189.
31. Runpu Hao, Eric Seth Michael, Franciszek Hennel, and Klaas Paul Pruessmann. Non-monotonic time- and frequency-dependent diffusion kurtosis in the human brain revealed by pulsed and oscillating gradient experiments. *Magnetic Resonance in Medicine*, (June): 1–16, jul 2025. ISSN 0740-3194. doi: 10.1002/mrm.30635.
32. Arthur Chakwizira, Filip Szczepankiewicz, and Markus Nilsson. Diffusion MRI with double diffusion encoding and variable mixing times disentangles water exchange from transient kurtosis. *Scientific Reports*, 15(1):8747, mar 2025. ISSN 2045-2322. doi: 10.1038/s41598-025-93084-4.
33. Dmitry S. Novikov, Jens H. Jensen, Joseph A. Helpern, and Els Fieremans. Revealing mesoscopic structural universality with diffusion. *Proceedings of the National Academy of Sciences*, 111(14):5088–5093, apr 2014. ISSN 0027-8424. doi: 10.1073/pnas.1316944111.
34. Hong-Hsi Lee, Antonios Papaioannou, Dmitry S. Novikov, and Els Fieremans. In vivo observation and biophysical interpretation of time-dependent diffusion in human cortical gray matter. *NeuroImage*, 129:414–427, jan 2020. ISSN 10959572. doi: 2001.06529v1.
35. Ileana O. Jelescu, Alexandre de Skowronski, Françoise Geffroy, Marco Palombo, and Dmitry S. Novikov. Neurite Exchange Imaging (NEXI): A minimal model of diffusion in gray matter with inter-compartment water exchange. *NeuroImage*, 256(April):119277, aug 2022. ISSN 10538119. doi: 10.1016/j.neuroimage.2022.119277.
36. Jonas L Olesen, Leif Østergaard, Noam Shemesh, and Sune N Jespersen. Diffusion time dependence, power-law scaling, and exchange in gray matter. *NeuroImage*, 251:118976, 2022.
37. Eloïse Mougel, Julien Valette, and Marco Palombo. Investigating exchange, structural disorder and restriction in gray matter via water and metabolites diffusivity and kurtosis time-dependence. *arXiv preprint arXiv:2306.16984*, 2023.

38. Marco Palombo, Clémence Ligneul, Chloé Najac, Juliette Le Douce, Julien Flament, Carole Escartin, Philippe Hantraye, Emmanuel Brouillet, Gilles Bonvento, and Julien Valette. New paradigm to assess brain cell morphology by diffusion-weighted mr spectroscopy in vivo. *Proceedings of the National Academy of Sciences*, 113(24):6671–6676, 2016.
39. Clémence Ligneul, Lily Qiu, William T Clarke, Saad Jbabdi, Marco Palombo, and Jason P. Lerch. Diffusion MRS tracks distinct trajectories of neuronal development in the cerebellum and thalamus of rat neonates. *eLife*, 13:1–20, oct 2025. ISSN 2050-084X. doi: 10.7554/eLife.96625.4.
40. Francesca Branzoli, Ece Ercan, Andrew Webb, and Itamar Ronen. The interaction between apparent diffusion coefficients and transverse relaxation rates of human brain metabolites and water studied by diffusion-weighted spectroscopy at 7 t. *NMR in Biomedicine*, 27(5): 495–506, 2014.
41. Christopher W. Davies-Jenkins, André Döring, Fabrizio Fasano, Elena Kleban, Lars Mueller, C John Evans, Maryam Afzali, Derek K Jones, Itamar Ronen, Francesca Branzoli, and Chantal M W Tax. Practical considerations of diffusion-weighted mrs with ultra-strong diffusion gradients. *Frontiers in Neuroscience*, 17, 12 2023. ISSN 1662-453X. doi: 10.3389/fnins.2023.1258408.
42. Axel Nimmerjahn, Frank Kirchhoff, and Fritjof Helmchen. Resting microglial cells are highly dynamic surveillants of brain parenchyma in vivo. *Science*, 308:1314–1318, 5 2005. ISSN 0036-8075. doi: 10.1126/science.1110647.
43. Soyon Hong, Victoria F. Beja-Glasser, Bianca M. Nfonoyim, Arnaud Frouin, Shaomin Li, Saranya Ramakrishnan, Katherine M. Merry, Qiaoqiao Shi, Arnon Rosenthal, Ben A. Barres, Cynthia A. Lemere, Dennis J. Selkoe, and Beth Stevens. Complement and microglia mediate early synapse loss in alzheimer mouse models. *Science*, 352:712–716, 5 2016. ISSN 0036-8075. doi: 10.1126/science.aad8373.
44. Paolo Calabresi, Alessandro Mechelli, Giuseppina Natale, Laura Volpicelli-Daley, Giulia Di Lazzaro, and Veronica Ghiglieri. Alpha-synuclein in parkinson's disease and other synucleinopathies: from overt neurodegeneration back to early synaptic dysfunction. *Cell Death & Disease*, 14:176, 3 2023. ISSN 2041-4889. doi: 10.1038/s41419-023-05672-9.
45. Jifei Miao, Haixia Ma, Yang Yang, Yuanpin Liao, Cui Lin, Juanxia Zheng, Muli Yu, and Jiao Lan. Microglia in alzheimer's disease: pathogenesis, mechanisms, and therapeutic potentials. *Frontiers in Aging Neuroscience*, 15, 6 2023. ISSN 1663-4365. doi: 10.3389/fnagi.2023.1201982.
46. Daniel Felsky, Tina Roostaei, Kwangsik Nho, Shannon L. Risacher, Elizabeth M. Bradshaw, Vlad Petyuk, Julie A. Schneider, Andrew Saykin, David A. Bennett, and Philip L. De Jager. Neuropathological correlates and genetic architecture of microglial activation in elderly human brain. *Nature Communications*, 10:409, 12 2019. ISSN 2041-1723. doi: 10.1038/s41467-018-08279-3.
47. Vaclav Brandejsky, Chris Boesch, and Roland Kreis. Proton diffusion tensor spectroscopy of metabolites in human muscle in vivo. *Magnetic Resonance in Medicine*, 73(2):481–487, feb 2015. ISSN 07403194. doi: 10.1002/mrm.25139.
48. Kadir Şimşek, André Döring, André Pampel, Harald E Möller, and Roland Kreis. Macromolecular background signal and <scp>non-Gaussian</scp> metabolite diffusion determined in human brain using ultra-high diffusion weighting. *Magnetic Resonance in Medicine*, (February):1–16, jul 2022. ISSN 0740-3194. doi: 10.1002/mrm.29367.
49. André Döring, Jessie Mosso, Roland Kreis, Nicholas G Dowell, Derek K Jones, Chloé Najac, Matt G Hall, Henrik Lundell, Lijing Xin, and Itamar Ronen. Robust double-diffusion-encoded spectroscopy (DDES) in the human brain on a clinical MR scanner using metabolite-cycling. In *Intl. Soc. Mag. Reson. Med.*, page 0645, 2024.
50. Karl Landheer, Kelley M. Swanberg, and Christoph Juchem. Magnetic resonance Spectrum simulator (MARSS), a novel software package for fast and computationally efficient basis set simulation. *NMR in Biomedicine*, (February):1–13, jul 2019. ISSN 0952-3480. doi: 10.1002/nbm.4129.
51. Patrik O. Wyss, Claudio Bianchini, Milan Scheidegger, Ioannis A. Giapitzakis, Andreas Hock, Alexander Fuchs, and Anke Henning. In vivo estimation of transverse relaxation time constant (T 2) of 17 human brain metabolites at 3T. *Magnetic Resonance in Medicine*, 80(2):452–461, aug 2018. ISSN 07403194. doi: 10.1002/mrm.27067.
52. Daniel G Q Chong, Roland Kreis, Christine S. Bolliger, Chris Boesch, and Johannes Slotboom. Two-dimensional linear-combination model fitting of magnetic resonance spectra to define the macromolecule baseline using FiTAID, a Fitting Tool for Arrays of Interrelated Datasets. *MAGMA*, 24(3):147–164, 2011. ISSN 09685243. doi: 10.1007/s10334-011-0246-y.
53. Victor Adalid, André Döring, Sreenath Pruthviraj Kyathanahally, Christine Sandra Bolliger, Chris Boesch, and Roland Kreis. Fitting interrelated datasets: metabolite diffusion and general lineshapes. *Magnetic Resonance Materials in Physics, Biology and Medicine*, 30 (5):429–448, oct 2017. ISSN 0968-5243. doi: 10.1007/s10334-017-0618-z.
54. Janez Stepišnik. Time-dependent self-diffusion by NMR spin-echo. *Physica B: Condensed Matter*, 183(4):343–350, may 1993. ISSN 09214526. doi: 10.1016/0921-4526(93)90124-O.
55. J Stepišnik. A new view of the spin echo diffusive diffraction in porous structures. *Europhysics Letters (EPL)*, 60(3):453–459, nov 2002. ISSN 0295-5075. doi: 10.1209/epl/i2002-00285-3.
56. Markus Nilsson, Filip Szczepankiewicz, Björn Lampinen, André Ahlgren, João P. de Almeida Martins, Samo Lasic, Carl-Fredrik Westin, and Daniel Topgaard. An open-source framework for analysis of multidimensional diffusion MRI data implemented in MATLAB. In *Intl. Soc. Mag. Reson. Med.*, page 5355, 2018.
57. P T Callaghan. A simple matrix formalism for spin echo analysis of restricted diffusion under generalized gradient waveforms. *Journal of Magnetic Resonance*, 129(1):74–84, nov 1997.
58. Ivana Drobnjak, Bernard Siow, and Daniel C. Alexander. Optimizing gradient waveforms for microstructure sensitivity in diffusion-weighted MR. *Journal of Magnetic Resonance*, 206 (1):41–51, sep 2010. ISSN 10907807. doi: 10.1016/j.jmr.2010.05.017.
59. Ivana Drobnjak, Hui Zhang, Matt G. Hall, and Daniel C. Alexander. The matrix formalism for generalised gradients with time-varying orientation in diffusion NMR. *Journal of Magnetic Resonance*, 210(1):151–157, may 2011. ISSN 10907807. doi: 10.1016/j.jmr.2011.02.022.
60. Andrada Ianuş, Bernard Siow, Ivana Drobnjak, Hui Zhang, and Daniel C. Alexander. Gaussian phase distribution approximations for oscillating gradient spin echo diffusion MRI. *Journal of Magnetic Resonance*, 227:25–34, 2013. ISSN 10907807. doi: 10.1016/j.jmr.2012.11.021.
61. Andrada Ianuş, Daniel C. Alexander, and Ivana Drobnjak. Microstructure Imaging Sequence Simulation Toolbox. In *IEEE Transactions on Medical Imaging*, volume 35, pages 34–44. oct 2016. ISBN 9783319466293. doi: 10.1007/978-3-319-46630-9_4.
62. Henrik Lundell, Chloé Najac, Marjolein Bulk, Hermien E. Kan, Andrew G. Webb, and Itamar Ronen. Compartmental diffusion and microstructural properties of human brain gray and white matter studied with double diffusion encoding magnetic resonance spectroscopy of metabolites and water. *NeuroImage*, 234(March):117981, jul 2021. ISSN 10538119. doi: 10.1016/j.neuroimage.2021.117981.
63. Robert Evans. The interpretation of small molecule diffusion coefficients: Quantitative use of diffusion-ordered NMR spectroscopy. *Progress in Nuclear Magnetic Resonance Spectroscopy*, 117:33–69, apr 2020. ISSN 00796565. doi: 10.1016/j.pnmrs.2019.11.002.